Geochemistry, Geophysics, Geosystems

RESEARCH ARTICLE
10.1029/2020GC009226

Key Points:
- The Christmas 2018 eruption of Mount Etna has been investigated through olivine chemical zoning, diffusion chronometry and geodetic data
- Data suggest prolonged recharge occurred since 6 months before the eruption and more importantly 3–16 days before Christmas 2018
- Pressure imbalances in the plumbing system now control the development of summit activity or flank eruptions at the volcano

Supporting Information:
- Table S1
- Table S2
- Table S3
- Data Set S1

Correspondence to:
M. Viccaro,
m.viccaro@unict.it

Citation:
Borzi, A. M., Giuffrida, M., Zuccarello, F., Palano, M., & Viccaro, M. (2020). The Christmas 2018 eruption at Mount Etna: Enlightening how the volcano factory works through a multiparametric inspection. *Geochemistry, Geophysics, Geosystems*, *21*, e2020GC009226. https://doi.org/10.1029/2020GC009226

Received 5 JUN 2020
Accepted 6 SEP 2020
Accepted article online 13 SEPT 2020

The Christmas 2018 Eruption at Mount Etna: Enlightening How the Volcano Factory Works Through a Multiparametric Inspection

Alfio Marco Borzi[1], Marisa Giuffrida[1], Francesco Zuccarello[1], Mimmo Palano[2], and Marco Viccaro[1,2]

[1]Dipartimento di Scienze Biologiche, Geologiche e Ambientali - Sezione di Scienze della Terra, Università degli Studi di Catania, Catania, Italy, [2]Istituto Nazionale di Geofisica e Vulcanologia - Sezione di Catania, Osservatorio Etneo, Catania, Italy

Abstract The 24–27 December 2018 flank eruption at Mount Etna (Southern Italy) has been investigated through a multidisciplinary approach in which olivine chemical zoning and diffusion chronometry data were integrated with models inferred by GNSS (Global Navigation Satellite System) measurements. Inspection of the olivine chemical zoning from core to rim allowed the identification of some dominant ways of transfer and interaction between magmas pertaining to different magmatic environments. Most of crystal cores are representative of crystallization at pressure of 290–230 and 160–120 MPa. Olivine rims suggest re-equilibration at shallow pressure (≤30 MPa). Geodetic-based models indicate pressurization of near-vertical prolate spheroidal sources centered at ~7.2 km below sea level (bsl) between 9 June 2017 and 28 June 2018 and later at ~5.1 km bsl between 28 June 2018 and the eruption onset. Geodetic data also highlight a change in the inflation rate since late June 2018 and later around November 2018, which has been here related to both replenishment phases and magma uprising across the plumbing system. Timescales of magma replenishment are in agreement with prolonged recharge from deep levels upward to shallow environments started about 6 months before the eruption, with further replenishment involving the upper magmatic environments just 3–16 days before the eruption. At present, the eruptive activity at the volcano is primarily controlled by pressure imbalances affecting extensive sections of the plumbing system, with possibility to develop persistent eruptive activity at the summit versus flank eruptions depending on fortuitous interruptions of the steady magma recharge/discharge rate at shallow levels.

1. Introduction

Monitoring geophysical networks on active volcanoes worldwide continuously deliver to the volcanological community huge amounts of high-quality data that are relevant for the comprehension of how magma moves into volcano plumbing systems. Four-dimensional constraining of magma movements is nowadays crucial for fixing two essential ambitions of the modern volcanology, that is, where and when an eruption might occur. Remarkable results in this regard can be hardly achieved through monodisciplinary, classical approaches of investigation, since they leave open multiple solutions for the most reliable interpretation of data. Definitely, cutting-edge polyhedral views of volcanic processes can be only conceived through merging of manifold disciplines (e.g., Fernández et al., 2017). Encouraging researches with this rationale have been already launched at some volcanoes on Earth, especially where products of the eruptive activity can be contextualized within the framework of data coming from high-quality monitoring networks (e.g., Carey et al., 2015; Cassidy et al., 2019; Geiger et al., 2016; Hibert et al., 2015; Magee et al., 2018; Martí et al., 2013).

Among these examples worldwide, Mount Etna is an exceptional candidate for promoting such kind of researches, due to the presence of an extensive multiparametric monitoring network installed on the volcano and for the continuous opportunity to cross-check models and ideas through the occurrence of new eruptive activity with an incredibly high frequency. Indeed, Mount Etna has been the site of recurrent eruptions over the last two decades from both the summit craters and the volcano flanks, with periods of entirely effusive activity changing to strongly explosive (i.e., violent Strombolian to lava fountains). Since 2011, the eruptive behavior has been mainly explosive with 44 paroxysmal eruptions that took place at the New South East Crater (NSEC) until December 2013 (Behncke et al., 2014; Giuffrida & Viccaro, 2017; Giuffrida

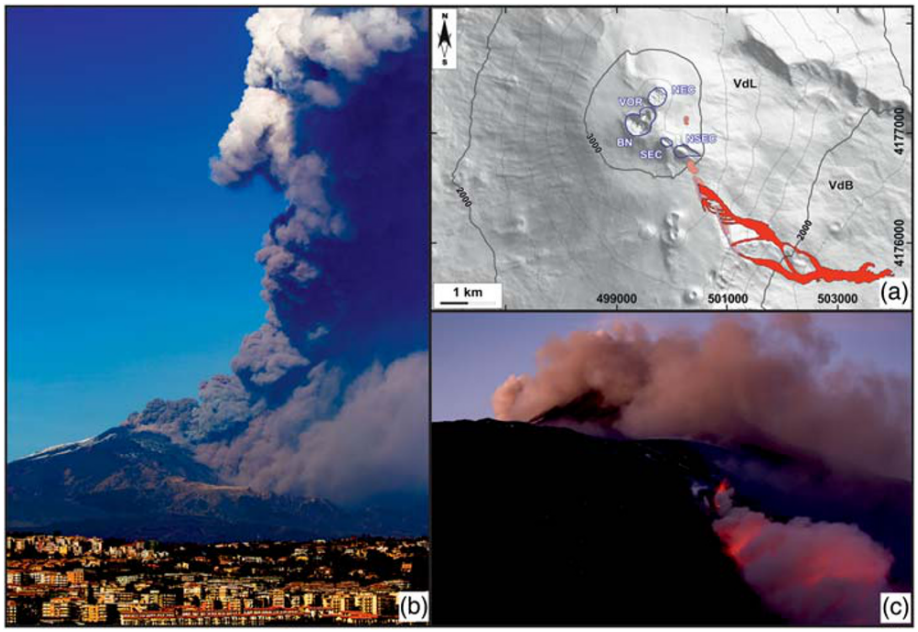

Figure 1. (a) Elevation model of the summit area of Mount Etna with scoria cones and eruptive fractures (pink areas) and the lava flow field (red areas) related to the December 2018 activity (INGV-OE Internal Report, 2019). VdB: Valle del Bove; VdL: Valle del Leone. The five summit craters are shown: Bocca Nuova (BN); Voragine (VOR); North East Crater (NEC); South East Crater (SEC); New South East Crater (NSEC). (b) Plume of dark ash during the early hours of the eruption on 24 December 2018. (c) View of the eruptive activity along the fissure opened on the western wall of the Valle del Bove during the afternoon of 24 December 2018.

et al., 2018; Viccaro et al., 2014, 2015). The activity drastically changed since 5 July 2014, with a prevalently effusive eruption at the North East Crater (NEC) and the NSEC lasting until 16 August 2014 (Viccaro, Zuccarello, et al., 2016). After the short-lived, effusive eruption of 31 January to 2 February 2015 from the NSEC, the activity moved at the Voragine (VOR) and gave rise on December 2015 and May 2016 to the most energetic, paroxysmal eruptions at Mount Etna throughout the last two decades (Aloisi et al., 2017; Bonaccorso & Calvari, 2017; Cannata et al., 2018; Corsaro et al., 2017). Ending of the paroxysmal activity at VOR on May 2016 marked a new change of the eruptive behavior, with the beginning of a period characterized by decrease of the eruptive frequency and activity being dominantly effusive, such as during the February–April 2017 eruptive events from the NSEC. In spite of the rather usual development of the eruption, the activity of 2017 at Mount Etna can be considered an archetype for emphasizing the importance of multidisciplinary studies in the detection of peculiar spatial and temporal dynamics at the volcano (Viccaro et al., 2019). Indeed, the interpretation of petrological and geodetic data alone provides a history of magma storage and transfer, which is virtually very simple until they are not mutually integrated.

This work develops on the same line of reasoning, dealing with the eruption of 24–27 December 2018 at Mount Etna, that is, the so-called "Christmas 2018 eruption" (Figure 1). We provide here an important data set taken on mineral phases, specifically olivine, found in the emitted products, which is combined with GNSS data, acquired by the Istituto Nazionale di Geofisica e Vulcanologia (INGV)-Osservatorio Etneo network, encompassing the 20 months preceding the eruption. Once again, we figure out an exceptional spatial and temporal reconstruction of magma movements into the volcano plumbing system prior to the eruption, advancing a model of how the volcano factory is working at present, especially for what concerns the conditions potentially leading to summit versus flank eruptions.

2. The Eruption of 24–27 December 2018 at Mount Etna

After about 15 months of rest since the February–April 2017 eruption, weak explosive activity resumed at Bocca Nuova (BN) and NEC on July 2018, culminating with the eruptive episode of 23–28 August 2018, when Strombolian explosions and lava flows took place at NSEC. Almost persistent very weak

Strombolian activity continued at BN, NEC, and NSEC during autumn 2018 without significant changes. Sudden signs of a forthcoming eruption at Mount Etna showed up at 07:30 GMT of 24 December 2018, after weeks of weak Strombolian activity and pulsating ash emission at NSEC, NEC and BN craters. The first sign was an important seismic swarm with thousands of events localized at depths of 0–3 km below the summit area, mostly in correspondence of the southeastern flank of the volcano (Alparone et al., 2020; Giampiccolo et al., 2020). At the same time, a plume of dark ash was observed at BN and NEC, reaching an altitude of 8–9 km above sea level (asl) and producing ash fallout southeastward (Figure 1b; Calvari et al., 2020; Corradini et al., 2020). The ash emission increased in a few hours and, at around 12:00 GMT, an eruptive fissure opened on the eastern side of the NSEC cone at an altitude of ~3,000 m asl, shortly followed by resumption of low-intensity explosive activity both at NEC and BN. Vigorous Strombolian explosions took place along the fissure, which rapidly propagated southeastward for about 3 km along a preexistent volcano-tectonic fracture formed in 1989 (Ferrucci et al., 1993), with the lowermost tip of the fissure reaching ~2,400 m asl (Figure 1c). During this initial phase of the eruption, several vents formed along the fracture, feeding a lava flow directed into the Valle del Bove. Lava effusions continued in the following days, producing a lava flow field on the western wall of Valle del Bove with maximum extension of ~5 km (Figure 1a). The lava emission at the fissure ended on 27 December, whereas the eruptive activity at BN ceased the next day.

Despite the eruption was rather small both in terms of duration and extension of the lava flow field, the entire eruptive phase was accompanied by an intense seismic swarm with a considerable number of high-energy seismic events with magnitude $M > 4$ between 24 and 27 December (Alparone et al., 2020; Giampiccolo et al., 2020). The strongest event with $M = 4.9$ occurred in the night between 25 and 26 December (at 2:19 GMT). It was responsible for heavy damages to buildings in several towns located in the southeastern sector of the volcano.

3. Petrological Data

3.1. Sampling and Analytical Methods

Fresh lava samples were taken during the first phase of the eruption on 24 December 2018. Five samples were collected in the summit area, right to the front of the active lava flow and rapidly quenched in order to minimize the effect of post-eruptive cooling. Air-quenched tephra were also collected during the entire duration of the eruption, between 24 and 27 December. Tephra were collected at different sites 7–8 km far from eruptive vents on the southeastern flank of the volcano.

Microanalyses on mineral phases were performed on polished thin sections of lavas and tephra at the Dipartimento di Scienze Biologiche, Geologiche e Ambientali of the University of Catania (Italy) using a Tescan Vega-LMU scanning electron microscope (SEM) equipped with an EDAX Neptune XM4-60 microanalyzer operating by energy dispersive system (EDS) characterized by an ultrathin Be window coupled with an EDAX WDS LEXS (wavelength dispersive low-energy X-ray spectrometer) calibrated for light elements. Operating conditions were set at 20 kV accelerating voltage and 2 nA for the analysis of major element abundances in mineral phases and 20 kV accelerating voltage and 8 nA to obtain high-contrast backscattered electron images (BSE 1024 × 864 pixels), especially for the inspection of olivine textures. Analytical spots were collected at the core and rim of plagioclases, clinopyroxenes, and opaque oxides, whereas olivine crystals were analyzed along core-to-rim traverses. We measured the Fo mol% variations [Fo mol% = 100 × Mg/(Mg + Fe + Mn)] in 52 olivine crystals from lavas and tephra. Analytical traverses were done along the shortest dimension of the olivine, perpendicular to one crystal face, and passing through the center of the crystal. Spacing between each spot analysis is in the order of 6–7 μm. Repeated analyses on internationally certified An-rich plagioclase, Fo-rich olivine, and glass inner standards during the analytical runs ensure precision of around 3–5% for all elements, while accuracy is ~5%. The complete microanalytical data set for crystals is available as Data Sets S1 and S2 in the supporting information.

3.2. Petrography and Mineral Chemistry of Volcanic Rocks

Lava samples show porphyritic index from ~25 to ~35 vol.%. The paragenesis is identical in all samples and consists of plagioclase (50–55 vol.%), clinopyroxene (20–30 vol.%), olivine (~15 vol.%), and Ti-magnetite (≤5 vol.%), occurring as both phenocrysts and microphenocrysts (<100 μm diameter), plus a microlite-bearing (mostly plagioclase) hyalopilitic groundmass. Large (0.2–2 mm) phenocrysts of euhedral to subhedral clinopyroxene and olivine are found in all rocks, where they form glomerophyric textures. Inclusions of

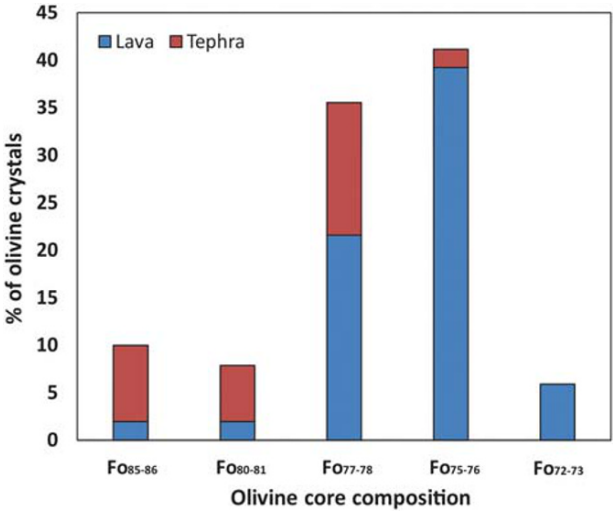

Figure 2. Percentage of olivine crystals characterized by distinct core compositions (compositional ranges in Fo mol%) in lava rocks and tephra of the 24–27 December 2018 eruption.

Ti-magnetite are common in both clinopyroxene and olivine. Plagioclase is more abundant but smaller in size (0.2 up to 1 mm) than clinopyroxene and olivine. Plagioclase phenocrysts are euhedral to anhedral and often show dissolution/resorption textures at the cores and/or rims. Plagioclase, clinopyroxene and olivine cover the same compositional range as their counterparts from other recently erupted magmas at Mount Etna since 2011 (Cannata et al., 2018; Giuffrida & Viccaro, 2017; Giuffrida et al., 2018; Viccaro et al., 2014, 2015, 2019; Viccaro, Zuccarello, et al., 2016; Viccaro, Barca, et al., 2016). Plagioclase phenocrysts show almost the same composition in all samples (core composition $An_{77–85}$ and rim composition $An_{66–71}$). Plagioclase microphenocrysts and microlites span over the same composition observed at the phenocryst rims. Clinopyroxene has Mg# [molar Mg/(Mg + Fe^{2+} + Mn)] ranging from 0.83 to 0.88 and augitic composition ($Wo_{44–47}$ $En_{46–49}$ $Fs_{7–9}$). Olivine crystals range in composition from Fo_{66} to Fo_{87}. However, cores are more homogeneous and mostly fall within the $Fo_{75–78}$ range (Figure 2; see the next section for further details).

Air-quenched tephra consist of ash fall deposits with clast sizes between 0.350 and 1 mm. Lithics constitute ~55% of the total fraction, whereas the juvenile fraction is ~45%. Most of the juvenile ash is sideromelane with typical fluidal morphology and interconnected tubular vesicles. Mineral phases in the juvenile clasts are 5–10 vol.% of the total volume. Even in the ashes, plagioclase, clinopyroxene, olivine, and Ti-magnetite form the mineral assemblage. Plagioclase and clinopyroxene are more abundant and larger (~1 mm in size) than olivine crystals, which are smaller than 0.5 mm. If compared to core compositions of olivine in lava rocks, olivine crystals from the fallout deposits are generally more forsteritic (Figure 2).

Details on the compositional variability of olivine crystals from both lava rocks and tephra are reported below.

3.3. Compositional Zoning of Olivine Crystals

Two types of olivine have been recognized from the examination of 52 crystals. The dominant type is zoned (around 76% of olivine phenocrysts). Single-step normal zoning is typically observed and characterizes the external portion of ~50% of the zoned crystals. Normally zoned olivines often have very thin (6–7 μm wide) zoned rims characterized by abrupt Fo decreases to $Fo_{72–75}$ (Figure 3a). Alternatively, they have thick zoned rims (up to 50 μm wide) along with the Fo content decreasing gradually to $Fo_{66–72}$ or Fo_{78} (Figure 3b). We recognized a slightly higher abundance of the former type. Among the zoned olivines, a minor population (~16% of phenocrysts) shows reversely zoned portions toward the rims. Reverse zoning patterns record Fo increase up to $Fo_{77–81}$, which is typically followed by normal zoning pattern toward the crystal rim (Figure 3c). In two cases, the reverse zoning is observed at the outer rim of olivine (Figure 3d). Core compositions of zoned crystals (normally or reversely zoned) are rather homogeneous, ranging between Fo_{75} and Fo_{78}. We have only found a few exceptions with respect to this range. These include two $Fo_{72–73}$ cores with reversely zoned rims, and nine cores at Fo_{80-81} and Fo_{84-86} for normally zoned olivines (Figure 2 and Data Set S2).

The second type of olivine crystals (~24% of the observed phenocrysts) is somewhat unzoned (Figures 3e and 3f). The entire core-to-rim profile of these crystals is characterized by very fine Fo oscillations, on the order of ~1 Fo mol% (Figure 3e). Some of these crystals display slight deflation of the Fo profile at the outermost rim (Figure 3f). Compositions mostly fall in the $Fo_{75–76}$ range (~16%) and $Fo_{77–78}$ (~5%), in accordance with the composition recorded at the core of zoned crystals (Figure 2).

4. Geodetic Data

Raw GNSS observations collected from the continuous geodetic network (Figure 4a) during the 15 March 2017 to 23 December 2018 time interval were analyzed by using the GAMIT/GLOBK software (Herring et al., 2018). According to Gonzalez and Palano (2014), absolute antenna phase centers models and precise

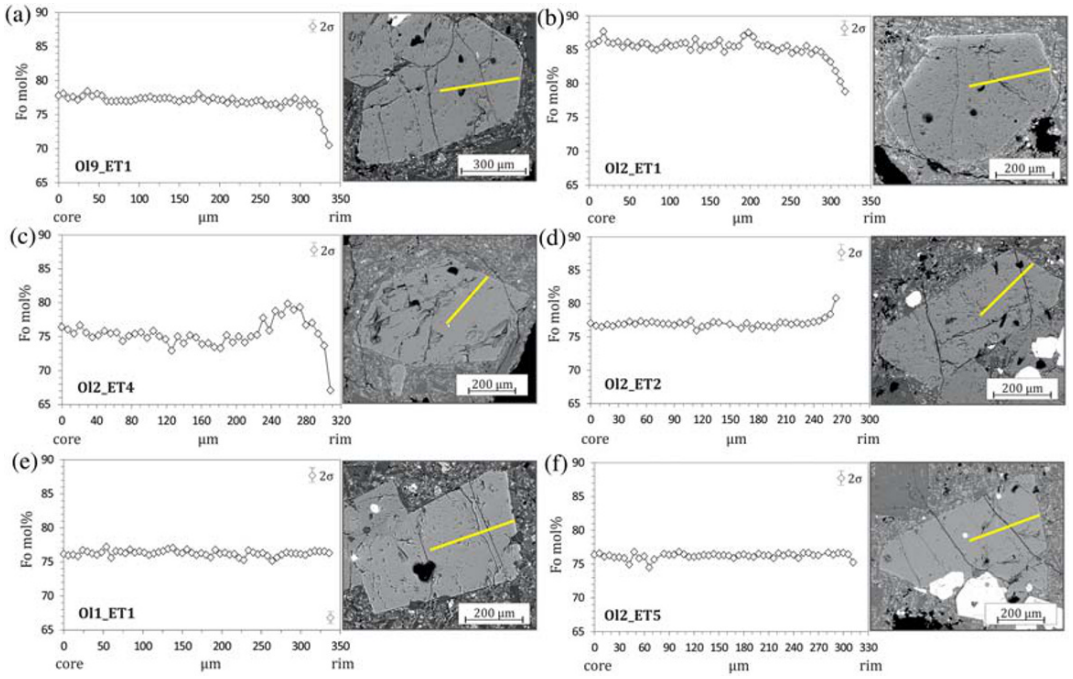

Figure 3. (a–f) Diagrams showing the dominant types of zoning in olivine crystals. Fo mol% = Forsterite mol% calculated as 100 × [Mg/(Mg + Fe + Mn)]. The 2σ error bars are shown in each plot. The direction of the core-to-rim compositional profile is drawn on olivine BSE images (yellow line).

ephemerides provided by the IGS (www.igs.org) were used. In addition, the Saastamoinen (1972) atmospheric zenith delay models, coupled with the Global Mapping Functions (Böhm et al., 2006) for the neutral atmosphere, have been also adopted. Results of this first step are estimations, on a daily base, of loosely constrained station coordinates and associated variance-covariance matrices which, in a successive step, were used as input in a Kalman filter to estimate a consistent set of daily coordinates (i.e., time series) for all sites involved. From these solutions we extracted all the baseline time series between all available couples of stations in order to easily detect, any significant signals related to magmatic activity of Mount Etna (Figures 4a and 4b). At Mount Etna, the daily baseline changes between couples of

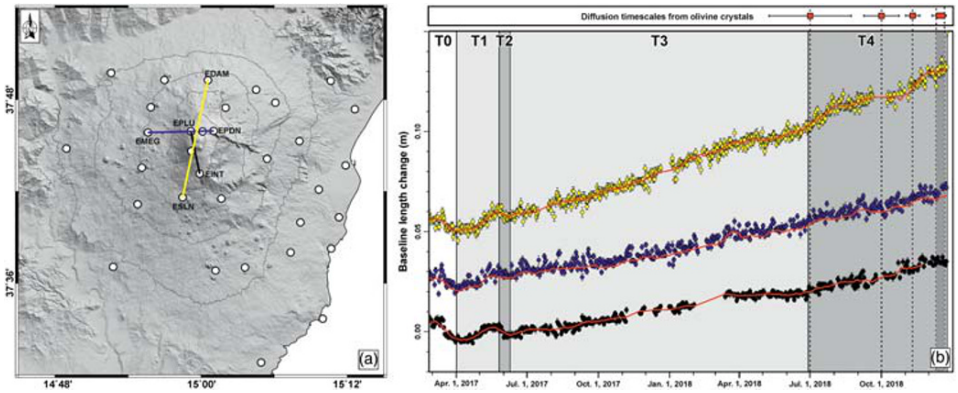

Figure 4. (a) Topographic map of Mount Etna with location of the GNSS stations used in this study. Station baselines shown in panel b are also reported. (b) Baseline time series of selected couples of stations (uncertainties at 95% interval): EDAM-ESLN (yellow points), EMEG-EPDN (blue points) and EPLU-EINT (black points). The red line represents the smoothed time series computed by applying a moving average filter with a time span of 10 days. The box at the top of baselines shows the distribution of diffusion timescales and their uncertainties throughout T4 (see section 5.2 for further details).

stations located on the upper portion of the volcano has been generally able to track the movement of magma along its plumbing system, as evidenced by numerous studies carried out in the last decades (e.g. Gonzalez & Palano, 2014; Palano et al., 2017; Viccaro et al., 2019, and references therein). Among all the available baseline time series, we focused on the daily baseline changes between some stations located on the upper portion of Mount Etna: EDAM-ESLN, EINT-EPLU, and EMEG-EPDN (Figure 4b). From the visual inspection of the baseline time series, we observed that the EMEG-EPDN baseline shows a homogeneous lengthening pattern over the 9 June 2017 to 23 December 2018 time interval, while the EDAM-ESLN and EINT-EPLU ones show some small changes on the lengthening pattern. For instance, a null to very small lengthening pattern (less than 4 mm) can be observed during 25 March to 28 June 2018 on the EINT-EPLU and EDAM-ESLN baselines. This last baseline also shows two short episodes of fast lengthening (~1 cm) during 28 June to 26 July 2018 and 7 November to 23 December 2018, respectively. Taking into account the most significant changes observed on all the analyzed baseline time series, we defined five main ground deformation stages. Such a subdivision allows us to estimate consistent ground deformation patterns (with high signal/noise ratio) of the whole GNSS network, providing a clear picture of magma movements along the plumbing system of the volcano. More in details, the baselines time series show shortening patterns during 15 March to 1 April 2017 (hereinafter T0) and 26 May to 9 June 2017 (hereinafter T2) and lengthening patterns during 1 April to 26 May 2017 (hereinafter T1), 9 June 2017 to 28 June 2018 (hereinafter T3), and 28 June to 23 December 2018 (hereinafter T4). For each detected stage, we estimated the ground deformation field (in terms of geodetic velocities) by combining the daily loosely solutions into a consistent set of station positions and velocities referred to the local Etn@ref reference frame (Palano et al., 2010). T0 stage has been already analyzed by Viccaro et al. (2019); interested readers can refer to this study for additional details. T2 is characterized by a general contraction of the upper part of the volcano edifice, indicating a depressurization of the volcano plumbing system (Figure 5), while T1, T3 and T4 show a general outward radial pattern, indicating a pressurization of the plumbing system (Figures 5 and 6).

We used the detected surface deformation patterns to constrain isotropic half-space elastic inversion models (see also the supporting information). We used the genetic algorithm method (e.g., Tiampo et al., 2000), adopting the Yang et al.'s (1988) analytical model and considering also the effects of topography (Williams & Wadge, 2000). The genetic algorithm works according to selection rules (as defined by the laws of evolutionary genetics), randomly selecting a set of models (in a wide range of model parameters values) and proceeds to evolve them in order to find the "best fit" model, that is, the model which produces surface deformations best matching the observed measurements. The "best fit" model is reached by minimizing the misfit defined as the root-mean-square error (RMSE):

$$\mathrm{RMSE} = \sqrt{\frac{\sum_{i=1}^{n} (P_i - O_i)^2}{n}}$$

where O_i and P_i represent the observed and predicted values respectively and n represents the number of data sets. The RMSE is a measure of the absolute fit of the model's predicted values to the observed data; lower values of RMSE indicate better fit. We assumed values of 30 GPa and 0.25 for the shear modulus and Poisson's ratio in the half-space, respectively. The rigidity chosen corresponds to a typical value of crustal rigidity commonly used in modeling works (e.g., Dzurisin, 2007; Williams & Wadge, 2000), which has been found to be an average rigidity value for Mount Etna crust (Chiarabba et al., 2000). We inverted both horizontal and vertical GNSS components with weights proportional to their associated uncertainties. Stations located on the middle-to-lower eastern flank of the volcano have been discarded from modeling because they are affected by long-term seaward motion (Palano, 2016). Parameters of the best fit models inferred for all the considered stages are reported in Table 1, whereas the modeled ground deformation patterns are reported in Figures 5 and 6.

The best fit source for T1 (RMSE of 14.4 mm/yr; Figures 5a and 5b) is located beneath the upper western flank of the volcano at a depth of ~5.1 km below sea level (bsl) and is given by an elongated spheroid body slightly dipping SW-ward with a positive volume change of 2.01×10^6 m^3 (Table 1). The best fit model for T2 (RMSE of 57.3 mm/yr; Figures 5c and 5d) is given by a near-vertical prolate spheroid source centered at ~3.8 km bsl beneath the western rim of the Valle del Bove depression and characterized by a negative volume change of 0.71×10^6 m^3 (Table 1). The best fit model for T3 (RMSE of 4.9 mm/yr; Figures 6a and

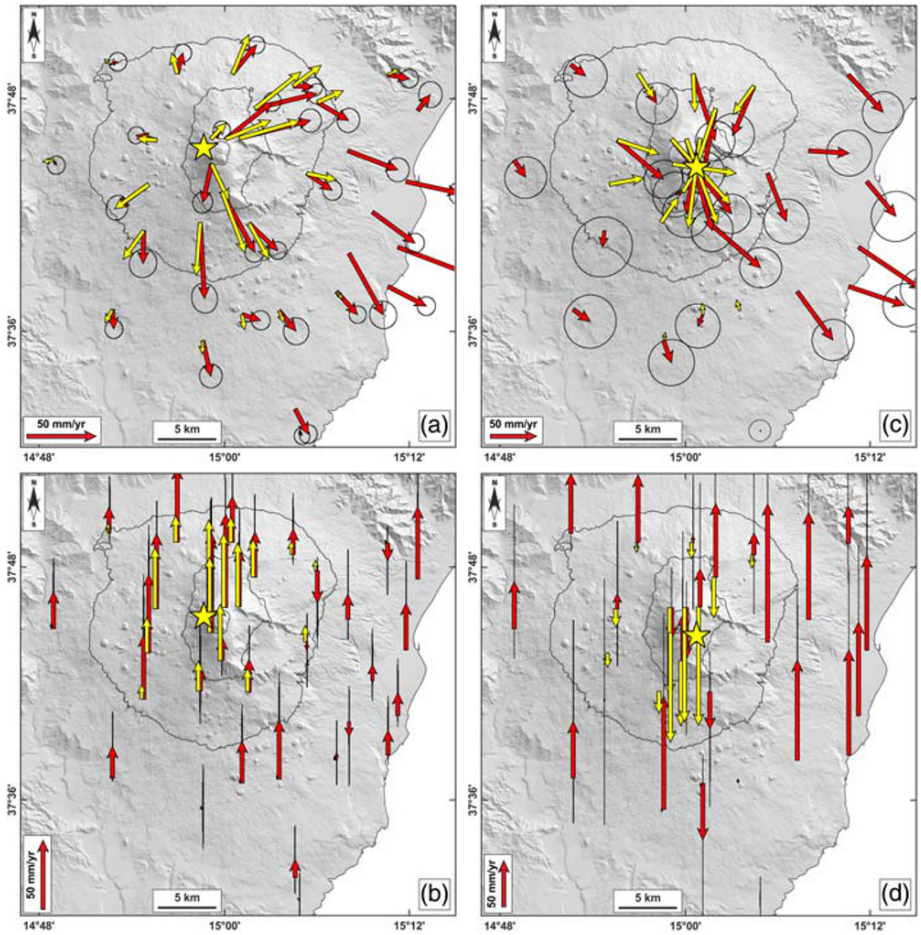

Figure 5. Comparison between observed (red arrows) and modeled (yellow arrows) horizontal (a and c) and vertical (b and d) ground deformation fields relevant to T1 (panels a and b; 1 April to 26 May 2017) and T2 (panels c and d; 26 May to 9 June 2017). The surface projections of modeled sources are reported as yellow stars. Parameters of the modeled sources are reported in Table 1.

6b) is given by a near-vertical prolate spheroid centered at ~7.0 km bsl beneath the NW side of summit area and is characterized by a positive volume change of 20.0×10^6 m^3 (Table 1). The best fit model for T4 (RMSE of 12.3 mm/yr; Figures 6c and 6d) is given by a near-vertical prolate spheroid centered at ~5.0 km bsl beneath the NW side of summit area and is characterized by a positive volume change of 5.8×10^6 m^3 (Table 1). The sources modeled for T1, T3, and T4 stages are well constrained, being the overall observed ground deformation patterns characterized by signals higher than the associated uncertainties. On the contrary, the source modeled for T2 is poorly constrained due to the low signal/noise ratio.

5. Discussion

5.1. Spatial Definition of the Volcano Plumbing System

The cores and rims of olivine crystals found in products of the 2018 eruption resemble well the range of olivine compositions already detected for other recent eruptions of Mount Etna (e.g., Cannata et al., 2018; Giuffrida & Viccaro, 2017; Viccaro et al., 2015, 2019; Viccaro, Zuccarello, et al., 2016). Specifically, the analysis of olivine core compositions and zoning pattern in volcanic rocks erupted since 2011 has led to group olivine crystals into six main populations, also constraining the thermodynamic parameters of the magmatic environments (M) in which a given population formed (e.g., Cannata et al., 2018; Giuffrida & Viccaro, 2017; Viccaro, Zuccarello, et al., 2016; Viccaro et al., 2019). The definition of P, T, and fO_2 of the identified magmatic environments follows the thermodynamic constraints provided by Giuffrida & Viccaro (2017),

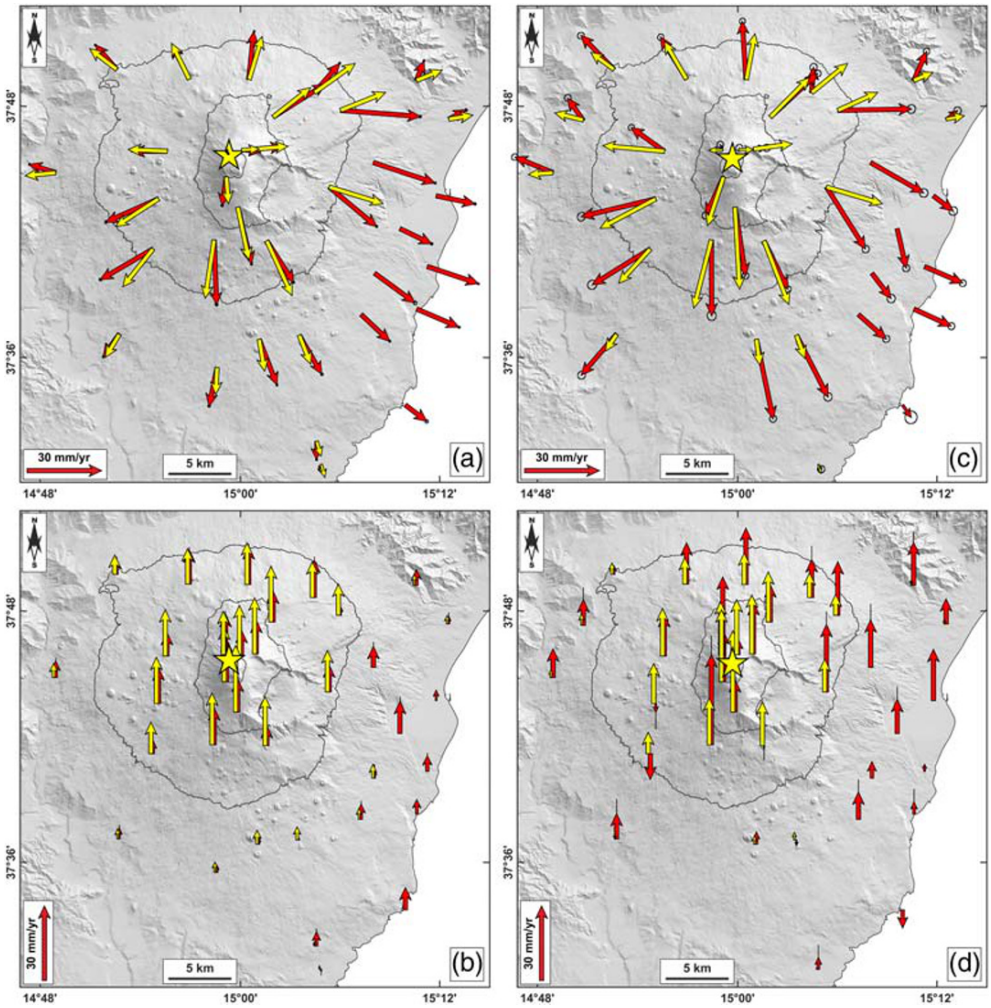

Figure 6. Comparison between observed (red arrows) and modeled (yellow arrows) horizontal (a and c) and vertical (b and d) ground deformation fields relevant to T3 (panels a and b; 9 June 2017 to 28 June 2018) and T4 (panels c and d; 28 June to 23 December 2018). The surface projections of modeled sources are reported as yellow stars. Parameters of the modeled sources are reported in Table 1.

which was performed by using the rhyolite-MELTS software (Ghiorso & Gualda, 2015; Gualda et al., 2012) for products of the 2011–2013 activity, and later reused also for the 2015–2016 and 2017 eruptive episodes (Cannata et al., 2018; Viccaro et al., 2019). Thermodynamic modeling accounts for the existence of magmatic environments (M_i) that are physically separated within the volcano plumbing system (Giuffrida & Viccaro, 2017; see also Figure 7). Previous studies stress how the same six olivine populations regularly occurred in volcanic products of Mount Etna during the last decade, providing clear evidence of selective reactivation of the these magmatic environments during the eruptive sequences of 2011–2013, 2014, 2015–2016 and 2017 (e.g., Cannata et al., 2018; Giuffrida & Viccaro, 2017; Viccaro, Zuccarello, et al., 2016; Viccaro et al., 2019). Novelty for the 24–27 December 2018 eruption is that almost all crystals are clustered at Fo_{78} and $Fo_{75–76}$ core compositions, which reflect magma storage and differentiation at the conditions of the M1a and M1b environments, respectively (Figure 7). However, our data indicate the presence of a number of intermediate terms between these two populations, with $Fo_{76–77}$ olivine cores highly represented in the data set. In spite of an overall compositional homogeneity of olivine cores, data support the presence of further populations of olivine crystals: (a) a low-Fo olivine population ($Fo_{72–73}$), which reflects the thermodynamic conditions of M2; (b) high-Fo populations (core compositions between Fo_{80} and Fo_{86}), which are consistent with thermodynamic conditions of M0 and M00. These are among

Table 1
Parameters of the Modeled Sources Inferred for Intervals Analyzed in This Study

Parameters	T1	T2	T3	T4
Easting (m)	498,092 ± 285	501,122 ± 178	498,934 ± 234	499,592 ± 277
Northing (m)	4,178,919 ± 195	4,177,068 ± 264	4,179,257 ± 288	4,178,981 ± 247
Depth (m bsl)	5,147 ± 312	3820 ± 304	7,180 ± 195	4,935 ± 326
a (m)	938.7 ± 131.4	673.7 ± 97.9	2,066.9 ± 120.6	1,646.8 ± 79.0
b/a ratio	0.25 ± 0.02	0.26 ± 0.02	0.21 ± 0.01	0.18 ± 0.01
Azimuth (°)	237.3 ± 11.5	178.7 ± 6.3	219.2 ± 11.4	11.20 ± 8.3
Dip (°)	34.1 ± 7.0	119.5 ± 6.8	79.4 ± 8.7	104.3 ± 6.8
ΔP (Pa)	$3.06 \pm 0.17 \cdot 10^8$	$-2.71 \pm 0.22 \cdot 10^8$	$3.97 \pm 0.20 \cdot 10^8$	$3.08 \pm 0.18 \cdot 10^8$
ΔV (10^6 m^3)	2.01 ± 1.76	−0.71 ± 0.57	20.01 ± 9.29	5.84 ± 2.81

Note. Estimation of the uncertainties in best fitting parameters was performed by adopting a Jackknife sampling method (Efron, 1982). The volume change of the ellipsoidal cavity has been estimated as (Battaglia et al., 2013): $\Delta V = \frac{3V\Delta P}{4\mu}\left(\frac{A^2}{3} - cA + d\right)$, where V is the volume of the ellipsoidal cavity, ΔP is the pressure change, $A = b/a$ represents the geometric aspect ratio between the semimajor axis a and the semiminor axis b of the Yang et al.'s (1988) analytical pressure source. Constants c and d are determined by the polynomial best fit to the numerical solutions provided from Amoruso and Crescentini (2009) and have values of 0.7 and 1.37, respectively. Coordinates are UTM33N.

the deepest and most basic environments observed in the volcano feeding system of Mount Etna during the last decade (Cannata et al., 2018; Giuffrida & Viccaro, 2017). Crystals reflecting the M_x environment have not been found in products of the 24–27 December 2018 eruption.

The petrological data set presented in this study shows evidence of a strong connection of M1a and M1b environments with the shallower M2, which is testified by the occurrence of normal zoning patterns in Fo_{78} and $Fo_{75–76}$ olivine crystals. Only few crystals record ascent and intrusion at shallow crustal levels of magmas more basic than M1a. For instance, reversely zoned crystals record the incorporation in the M0 magma, and subsequent reequilibration at the condition of M1a, M1b, or M2 magmas. Minor evidence also exists for the ascent of Fo_{86} olivine crystals, which come from a deep section of the plumbing system (i.e., the M00 environment; >600 MPa) toward the M2 environment.

The correlation of petrological and geodetic models has already put into evidence good correspondence between the M1a and M1b environments with geodetically inferred magmatic sources of deformation based on depths and associated uncertainties estimated for the 2015–2016 and 2017 volcanic events (Cannata et al., 2018; Viccaro et al., 2019). The active source inferred for the inflation and deflation deformative stages of the 2015–2016 activity at VOR was estimated at depth of ~4.6 km bsl, hence covering the same pressure range of M1b (Cannata et al., 2018). Differently, the source inferred for the inflation stage leading to the 2017 volcanic events lays closer to M1a, at depth of ~6.3 km bsl. Then, the source moved upward, overlapping M1b, during the second phase of the eruption between mid-March and April 2017 (Viccaro et al., 2019).

Moreover, geodetic data modeled during T1 (1 April to 26 May 2017) and T2 (26 May to 9 June 2017) stages suggest the occurrence of a short inflation/deflation cycle occurring along the volcano plumbing system at the depth range of M1b. These sources, coupled with the one observed during T0 (15 March to 1 April 2017; Viccaro et al., 2019), clearly highlight the primary role of M1b in feeding the 2017 volcanic activity (Figure 8a). During T3 (9 June 2017 to 28 June 2018), the geodetic data suggest a near-vertical magmatic reservoir centered at depth of ~7.2 km bsl, while during T4 (28 June to 23 December 2018), the modeled source is centered beneath the summit area at depth of ~5.1 km bsl. Based on their dimensions and position, source modeled for T3 and T4 are spatially intersecting/overlapping, defining a near-vertical portion of the volcano plumbing system placed between the M1a and M1b environments, which was interested by magma replenishment before the December 2018 eruptive event.

5.2. Temporal Reconstruction of Magma Replenishment and Transfer

Processes of magma transfer and interaction preceding the Christmas 2018 eruption are well evidenced by the chemical heterogeneities of olivine crystals. Modeling the diffusive relaxation of the Fe-Mg zoning in olivine allows the extraction of timescales associated to these processes. Chemical zoning in magmatic crystals typically originates from changes in temperature, pressure, and oxygen fugacity of the host environment, which in turn may result in crystal growth (or dissolution) and/or chemical diffusion. This means that the

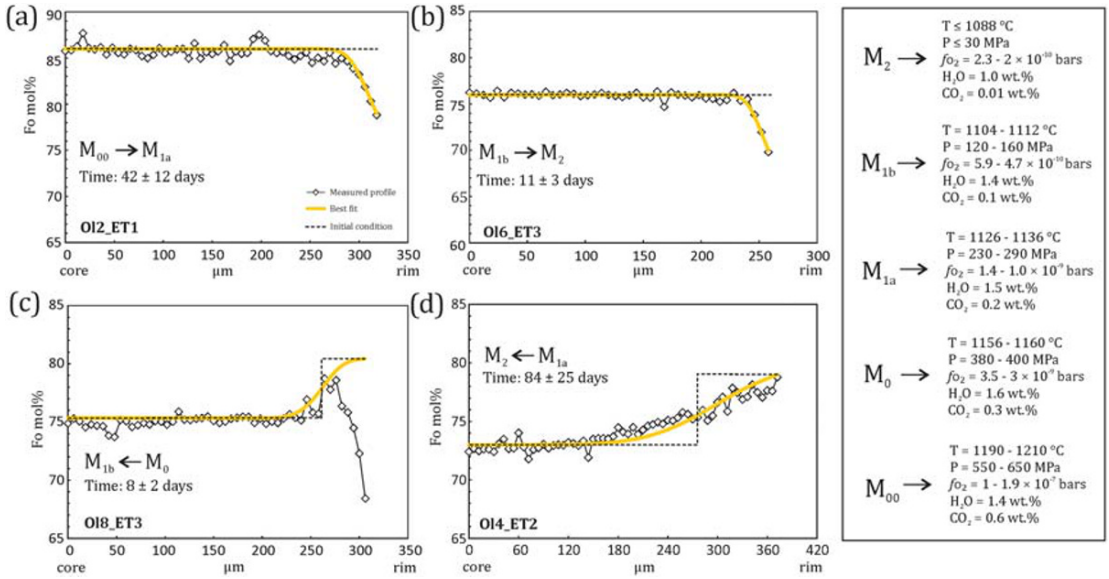

Figure 7. Application of Fe-Mg diffusion modeling for representative olivine crystals found in the Christmas 2018 erupted products. Best fit diffusion curves (yellow lines), initial distribution profile (dashed black lines), and resulting timescales are illustrated for crystals showing interactions between chemically distinct magmatic environments (M). The box on the right reports physical and chemical parameters resulting from rhyolite-MELTS simulations (cf. Giuffrida & Viccaro, 2017).

extraction of timescales by modeling chemical zoning in natural crystals often introduces a need to discriminate between the contribution of growth and diffusion on the final Fe-Mg zoning. Because the mutual effect of both mechanisms can hardly be discerned without recurring to the distribution of elements that diffuse at different rates, we have used a simple diffusion-only model (Costa et al., 2008) to

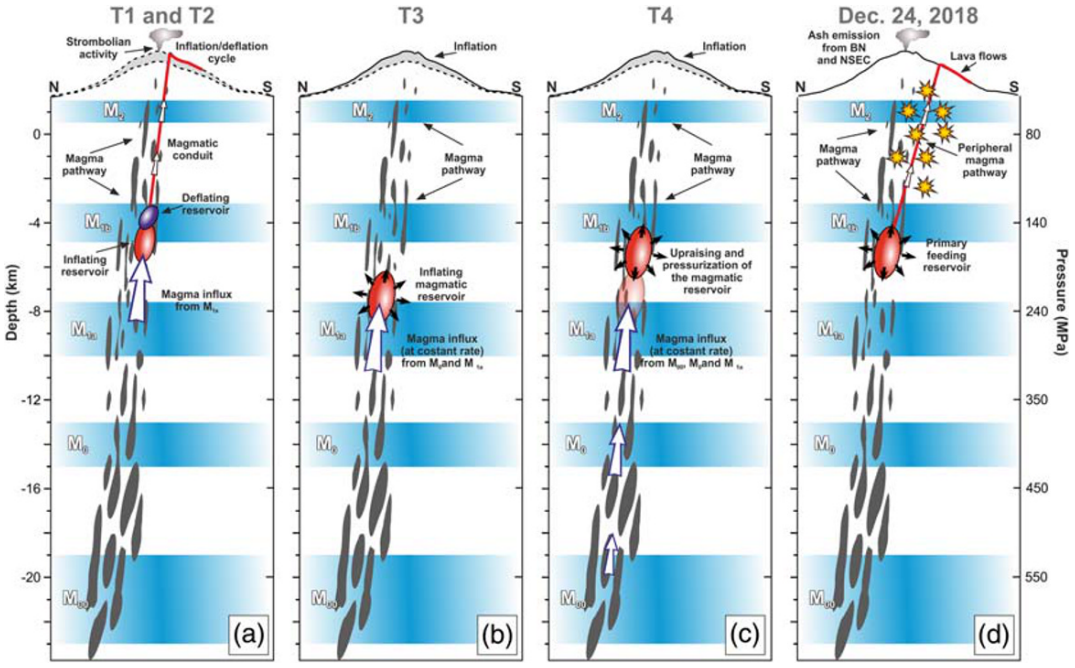

Figure 8. Schematic cartoons of magma movements and deformation sources within the Mount Etna plumbing system during (a) T1-T2 (1 April to 9 June 2017), (b) T3 (9 June 2017 to 28 June 2018), (c) T4 (28 June to 23 December 2018), and (d) 24 December 2018. Inflation and deflation sources are reported in red and in blue, respectively. The magmatic environments with associated pressure and depth ranges are from Giuffrida & Viccaro (2017).

track the chemical relaxation of Fe-Mg over time. The modeling assumes that diffusion had larger impact than growth on the final shape of the concentration profile and does not account for changes in temperature and boundary conditions with time. As a consequence, we have used a homogeneous concentration profile as initial distribution in normally zoned crystals. Instead, a step-like initial distribution has been applied to one single normally zoned crystal (i.e., Ol10_ET1) that shows two subsequent stages of growth in differently evolved magma volumes. A step-like initial profile was also adopted for modeling the reversely zoned crystals where the Fo gradient is supposed originating from diffusive exchange after incorporation of the olivine in a recharging magma of more basic composition. The concentration profiles were modeled numerically by using the method of finite difference (Costa et al., 2008; Costa & Morgan, 2010; see Figure 7 and Data Set S3). The crystal boundaries were considered to be open and, in all instances, the concentration was held constant at crystal rim assumed to be in equilibrium with the surrounding melt. Fe-Mg diffusion coefficients ($D_{Fe\text{-}Mg}$; Dohmen & Chakraborty, 2007) were determined for a given olivine population by using the T, P, and fO_2 parameters that define a physical environment consistent with the range of crystallization conditions recognized at Mount Etna for the post-2011 activity (Giuffrida & Viccaro, 2017). Diffusion coefficients were initially calculated parallel to [001] (Dohmen & Chakraborty, 2007). Due to the strong diffusion anisotropy of olivine, the $D_{Fe\text{-}Mg}$ value was corrected for the profile direction (D_{trav}) by taking into account the orientation of the chemical profile relative to the crystallographic axes of the olivine (Costa & Chakraborty, 2004). Olivine a, b, and c axes were measured by conoscopic observations under a polarizing optical microscope equipped with a Zeiss 4 axis universal stage. Concentration profiles obtained from randomly sectioned olivine crystals were not modeled. Rather, crystals were preliminarily selected on polished thin sections based on the orientation of the olivine plane with respect to the fast diffusion direction (i.e., c axis; Costa & Chakraborty, 2004; Shea et al., 2015). For each olivine detected at the optical microscope, we measured the angle between the section of the olivine plane and the c axis. Only crystals with an angle <45° between the olivine plane and c axis were selected for the diffusion model. This choice follows criteria introduced by Costa & Chakraborty (2004) and Shea et al. (2015), which allow reducing uncertainties on time determinations. Uncertainties on timescales were calculated by propagating the error in the diffusion coefficient determination, which is primarily governed by changes in temperature and oxygen fugacity. We used standard procedures for error propagation analysis, following the method described in Kahl et al. (2015). The error propagation analysis was therefore performed for a given olivine population by fixing temperature and fO_2 uncertainties starting from the thermodynamic conditions of crystallization fixed for each magmatic environment. It is worth noting that under the assumption of a diffusion-only contribution (using homogeneous or step-like initial conditions) on the observed zoning profiles, the modeling yields timescales longer than those potentially obtained by a diffusion plus growth model. The advantage is that such an approach allows simplifying a complex magmatic situation that likely involves non-isothermal diffusion and moving boundary conditions during the transfer of the crystal from a magmatic environment to another. It is also worth to consider that obtained timescales are within the resolvable limits introduced by Bradshaw and Kent (2017), being the ratio between the gradient width and the spot size higher than 2. The robustness of our assumptions also relies on the fact that diffusion curves fit particularly well most of measured profiles without invoking changes in temperature and boundary conditions with time, thus confirming the dominant role of diffusion in producing olivine zoning.

Based on our results, Fo_{78} and $Fo_{75–76}$ olivine crystals related to the M1a (Fo_{78}) and M1b ($Fo_{75–76}$) experienced diffusive relaxation over timescales of 4–16 days during the transfer and residence in the shallow M2 ($Fo_{72–73}$) environment (Table 2). Moreover, the diffusive reequilibration for most of the observed reverse zoning patterns reproduces intrusion of magmas from M0 into M1a and M1b, which occurred over comparable timescales, that is, 3–11 days before the eruption (Table 2). In this regard, a delay between the time of intrusion and the time in which the entrained crystal cargo responds could have affected these short timescales (cf. Cheng et al., 2020). However, although most of olivines record a short-term history (i.e., 3–16 days) of ascent and interaction before the Christmas 2018 eruption, the occurrence of residual crystals registering timescales in the order of several months also suggests long-term processes of magma recharge. These features are in accordance with deformation data.

The inflating source feeding the 2017 volcanic events was close to M1a, at depth of ~6.3 km bsl, and moved upward during the second phase of the eruption, depicting an inflation/deflation cycle, overlapping M1b between mid-March and April 2017 (Figure 8a; cf. Viccaro et al., 2019). During T1 and T2 stages (Table 1)

Table 2
Diffusion Modeling Results for Olivine Crystals

Sample	T (°C)	P (MPa)	fO_2 (bars)	M	$\Delta t \pm \sigma$
OL2_ET1	1131	260	$10^{-8.92}$	M00-M1a (n)	42 ± 13
OL7_ET1	1084	30	$10^{-9.65}$	M1a-M2 (n)	11 ± 3
OL8_ET1	1084	30	$10^{-9.65}$	M1a-M2 (n)	16 ± 5
OL9_ET1	1084	30	$10^{-9.65}$	M1a-M2 (n)	8 ± 3
OL10_ET1	1108	140	$10^{-9.28}$	M0-M1b (n)	176 ± 54
OL2_ET2	1158	260	$10^{-8.49}$	M1a-M0 (r)	3 ± 1
OL3_ET2	1084	30	$10^{-8.92}$	M1a-M2 (n)	5 ± 2
OL4_ET2	1131	30	$10^{-8.92}$	M2-M1a (r)	84 ± 25
OL3_ET3	1084	30	$10^{-9.28}$	M1b-M2 (n)	6 ± 2
OL2_ET3	1084	30	$10^{-8.92}$	M1a-M2 (n)	8 ± 3
OL6_ET3	1084	30	$10^{-9.28}$	M1b-M2 (n)	11 ± 3
OL7_ET3	1084	30	$10^{-9.28}$	M1b-M2 (n)	16 ± 5
OL8_ET3	1158	140	$10^{-8.49}$	M1b-M0 (r)	8 ± 2
OL9_ET3	1084	30	$10^{-8.92}$	M1a-M2 (n)	4 ± 1
OL2_ET4	1158	140	$10^{-9.28}$	M1b-M0 (r)	11 ± 3

Note. Timescales (days) and relative uncertainties (2σ) were calculated for distinct zoned portions of a crystal (n: normal; r: reverse), each indicating a given connection between two magmatic environments (M). Thermodynamic conditions used for the modeling are also shown. All modeled olivine crystals are from lava flows.

another inflation/deflation cycle occurred at the same depth range of the previous one. Both cycles have marked the fast ascent of magma from deep reservoirs, which caused restoration of the pressure balance throughout the shallowest portion of the volcano plumbing system (from M1b upward the surface). This could explain why volcanic activity was almost absent for a considerable period of time since the end of the 2017 eruption. Geodetic data clearly detected a main episode of two-step inflation that started on late June 2017, involving two contiguous vertically elongated portions of the plumbing system. During T3, the modeled source was centered at a depth of ~7.2 km bsl and experienced vigorous pressurization (Figure 8b). In particular, this part of the plumbing system was refilled at a constant rate for a prolonged period by new magma, as suggested by the linear trend of analyzed baseline time series (Figure 4) and by the presence of one olivine registering intrusion processes with timescales of 6 months (Table 2). This long-term recharge has been probably consequential for re-establishing the pressure balance for this portion of the plumbing system. During T4, the modeled source was located at depth of ~5.1 km bsl, spatially intersecting/overlapping the upper part of the T3 source, therefore defining a near-vertical portion of the volcano plumbing system (Figure 8c). Such a portion was interested by conspicuous magma recharge at an average rate of 0.05×10^6 and 0.03×10^6 m^3/day during T3 and T4, respectively. However, as previously mentioned, such a rate was not constant over time, especially throughout T4. More in detail, the rate increased since June 2018 (beginning of T4) and later again since 7 November 2018 (Figure 4), as also suggested by the presence of an olivine registering intrusion 42 days before the Christmas 2018 eruption (Table 2 and Figure 4). This feature has been here ascribed to an intensified rate of replenishment by new magma involving the plumbing system, which has finally led to the eruption run-up in the 2 weeks preceding the Christmas 2018. This inference also appears consistent with the SO_2 flux data reported by Calvari et al. (2020), who put into evidence mean flux values higher than those typical of quiescent regimes at the volcano since late November 2018 and, more prominently, during the 10 days preceding the eruption.

One last consideration regards the final upward magma migration with activation of M2. This environment is virtually absent in olivine cores of the 2018 volcanic products, but is largely represented in olivine rims (Figure 3 and Data Set S2). Lacks of olivine cores pertaining to M2 is rather odd, being this very shallow environment ubiquitously activated throughout the eruptions of the last decade. This distinguishing characteristic should be related to bypassing of the shallow central conduit and re-equilibration of olivine rims at the M2 thermodynamic conditions in a spatially different position of the volcano edifice (Figure 8d). This inference definitely agrees with development of the eruptive activity along the southeastern flank of the volcano, which has been accounted for as due to a dike intrusion departing from the central conduit system (e.g., Bonforte et al., 2019; Cannavò et al., 2019; De Novellis et al., 2019; Giampiccolo et al., 2020; Pezzo et al., 2020). Timing for re-equilibration to M2 conditions suggests that this lateral intrusion into the volcano southeastern flank started from the M1b level just a few days before the eruption.

6. Conclusions

The multiparametric study of the so-called Christmas 2018 flank eruption of Mount Etna volcano allowed a thorough reconstruction of the storage and transfer dynamics preceding the eruption, which date back to the end of the 2017 eruptive activity. More consistent reactivation of the plumbing system has been detected since June 2017, with a prolonged period of inflation due to magma replenishment and pressurization into a reservoir located at ~7.2 km bsl. Magma ascent was observed since June 2018, when magma migrated and pressurized a reservoir located at ~5.1 km bsl and in early November, when magma started its progressive migration toward the surface. This continuous replenishment and storage at deep/intermediate levels of the plumbing system of Mount Etna, coupled with very limited transfer at shallow levels, must be viewed as the main cause for accumulation of huge stresses in the volcanic edifice.

How the Christmas 2018 eruption should be considered within the framework of the eruptive record of the last decade is not, however, a simple task. If the period 2011–2014 has been mainly characterized by frequent, short-lasting paroxysmal eruptions fed by short-term accumulation of magmas chiefly into the shallow portions of the plumbing system, the activity since December 2015 appears more consistent with prolonged replenishment and storage dynamics involving the deepest levels of the volcano. At present, possibility for magma transfer and drainage at shallower levels seems to be therefore controlled by pressure imbalances that trigger self-feeding processes of recharge, as during the 2017 eruption. If accidental interruptions of the steady magma recharge/discharge rate occur at shallow levels, the plumbing system is able to pressurize at high-intermediate depth, which is a feature preluding the development of flank eruptions at the volcano. The Christmas 2018 flank eruption suggests that a fortuitous interruption of this steady state could have occurred at the end of the 2017 eruption (conduit and/or eastern flank spreading dynamics?). However, the still ongoing activity at VOR and NSEC craters since September 2019 could suggest that the steady state allowing magma drainage at shallow levels has been restored in some way after the Christmas 2018 eruption.

Conflict of Interest

The authors declare no financial or other conflicts of interests.

Data Availability Statement

The GNSS data presented and analyzed in this article are freely available online (at the link https://www.doi.org/10.6084/m9.figshare.12928865).

Acknowledgments

This work was supported by the funding program of the University of Catania through the Three Year Plan 2016–2018 Project Code 22722132140 and the Three Year Plan 2020–2022 Project Code 22722132140 (project coordinator M. Viccaro). We are indebted to D. Pellegrino, M. Pulvirenti and M. Rossi, technicians of the INGV - Osservatorio Etneo, for maintenance, implementation and data acquisition of the continuous GNSS network. Finally, we are thankful to M. Edmonds for the handling of our manuscript, to B. Gordeychik and two anonymous reviewers for their helpful comments and suggestions.

References

Aloisi, M., Jin, S., Pulvirenti, F., & Scaltrito, A. (2017). The December 2015 Mount Etna eruption: An analysis of inflation/deflation phases and faulting processes. *Journal of Geodynamics*, *107*, 34–45. https://doi.org/10.1016/j.jog.2017.03.003

Alparone, S., Barberi, G., Giampiccolo, E., Maiolino, V., Mostaccio, A., Musumeci, C., et al. (2020). Seismological constraints on the 2018 Mt. Etna (Italy) flank eruption and implications for the flank dynamics of the volcano. *Terra Nova*, 1–11. https://doi.org/10.1111/ter.12463

Amoruso, A., & Crescentini, L. (2009). Shape and volume change of pressurized ellipsoidal cavities from deformation and seismic data. *Journal of Geophysical Research*, *114*, B02210. https://doi.org/10.1029/2008JB005946

Battaglia, M., Cervelli, P. F., & Murray, J. R. (2013). DMODELS: A MATLAB software package for modeling crustal deformation near active faults and volcanic centers. *Journal of Volcanology and Geothermal Research*, *254*, 1–4. https://doi.org/10.1016/j.jvolgeores.2012.12.018

Behncke, B., Branca, S., Corsaro, R. A., De Beni, E., Miraglia, L., & Proietti, C. (2014). The 2011–2012 summit activity of Mount Etna: Birth, growth and products of the new SE crater. *Journal of Volcanology and Geothermal Research*, *270*, 10–21. https://doi.org/10.1016/j.jvolgeores.2013.11.012

Böhm, J., Werl, B., & Schuh, H. (2006). Troposphere mapping functions for GPS and very long baseline interferometry from European Centre for Medium-Range Weather Forecasts operational analysis data. *Journal of Geophysical Research*, *111*, B02406. https://doi.org/10.1029/2005JB003629

Bonaccorso, A., & Calvari, S. (2017). A new approach to investigate an eruptive paroxysmal sequence using camera and strainmeter networks: Lessons from the 3–5 December 2015 activity at Etna volcano. *Earth and Planetary Science Letters*, *475*, 231–241. https://doi.org/10.1016/j.epsl.2017.07.020

Bonforte, A., Guglielmino, F., & Puglisi, G. (2019). Large dyke intrusion and small eruption: The December 24, 2018 Mt. Etna eruption imaged by Sentinel-1 data. *Terra Nova*, *31*(4), 405–412. https://doi.org/10.1111/ter.12403

Bradshaw, R. W., & Kent, A. J. (2017). The analytical limits of modeling short diffusion timescales. *Chemical Geology*, *466*, 667–677. https://doi.org/10.1016/j.chemgeo.2017.07.018

Calvari, S., Bilotta, G., Bonaccorso, A., Caltabiano, T., Cappello, A., Corradino, C., et al. (2020). The VEI 2 Christmas 2018 Etna eruption: A small but intense eruptive event or the starting phase of a larger one? *Remote Sensing*, *12*(6), 905. https://doi.org/10.3390/rs12060905

Cannata, A., Di Grazia, G., Giuffrida, M., Gresta, S., Palano, M., Sciotto, M., et al. (2018). Space-time evolution of magma storage and transfer at Mt. Etna volcano (Italy): The 2015–2016 reawakening of Voragine crater. *Geochemistry, Geophysics, Geosystems*, *19*, 471–495. https://doi.org/10.1002/2017GC007296

Cannavò, F., Sciotto, M., Cannata, A., & Di Grazia, G. (2019). An integrated geophysical approach to track magma intrusion: The 2018 Christmas Eve eruption at Mount Etna. *Geophysical Research Letters*, *46*, 8009–8017. https://doi.org/10.1029/2019GL083120

Carey, R., Cayol, V., Poland, M., & Weis, D. (2015). *Hawaiian volcanoes: From source to surface* (p. 600). Geophysical Monograph Series, Washington, D. C: American Geophysical Union. https://doi.org/10.1002/9781118872079

Cassidy, M., Ebmeier, S. K., Helo, C., Watt, S. F. L., Caudron, C., Odell, A., et al. (2019). Explosive eruptions with little warning: Experimental petrology and volcano monitoring observations from the 2014 eruption of Kelud, Indonesia. *Geochemistry, Geophysics, Geosystems*, *20*, 4218–4247. https://doi.org/10.1029/2018GC008161

Cheng, L., Costa, F., & Bergantz, G. (2020). Linking fluid dynamics and olivine crystal scale zoning during simulated magma intrusion. *Contributions to Mineralogy and Petrology*, *175*(6), 53. https://doi.org/10.1007/s00410-020-01691-3

Chiarabba, C., Amato, A., Boschi, E., & Barberi, F. (2000). Recent seismicity and tomographic modeling of the Mount Etna plumbing system. *Journal of Geophysical Research*, *105*(B5), 10,923–10,938. https://doi.org/10.1029/1999JB900427

Corradini, S., Guerrieri, L., Stelitano, D., Salerno, G., Scollo, S., Merucci, L., et al. (2020). Near real-time monitoring of the Christmas 2018 Etna eruption using SEVIRI and products validation. *Remote Sensing*, *12*(8), 1336. https://doi.org/10.3390/rs12081336

Corsaro, R. A., Andronico, D., Behncke, B., Branca, S., Caltabiano, T., Ciancitto, F., et al. (2017). Monitoring the December 2015 summit eruptions at Mt. Etna (Italy): Implications on eruptive dynamics. *Journal of Volcanology and Geothermal Research*, *341*, 53–69. https://doi.org/10.1016/j.jvolgeores.2017.04.018

Costa, F., & Chakraborty, S. (2004). Decadal time gaps between mafic intrusion and silicic eruption obtained from chemical zoning patterns in olivine. *Earth and Planetary Science Letters*, *227*(3–4), 517–530. https://doi.org/10.1016/j.epsl.2004.08.011

Costa, F., Dohmen, R., & Chakraborty, S. (2008). Timescales of magmatic processes from modeling the zoning patterns of crystals. *Reviews in Mineralogy and Geochemistry*, *69*(1), 545–594. https://doi.org/10.2138/rmg.2008.69.14

Costa, F., & Morgan, D. J. (2010). Time constraints from chemical equilibration in magmatic crystals. In A. Dosseto (Ed.), *Timescales of magmatic processes: From core to atmosphere* (pp. 125–159). West Sussex, UK: John Wiley. https://doi.org/10.1002/9781444328509.ch7

De Novellis, V., Atzori, S., De Luca, C., Manzo, M., Valerio, E., Bonano, M., et al. (2019). DInSAR analysis and analytical modeling of Mount Etna displacements: The December 2018 volcano-tectonic crisis. *Geophysical Research Letters*, *46*, 5817–5827. https://doi.org/10.1029/2019GL082467

Dohmen, R., & Chakraborty, S. (2007). Fe-Mg diffusion in olivine II: Point defect chemistry, change of diffusion mechanisms and a model for calculation of diffusion coefficients in natural olivine. *Physics and Chemistry of Minerals*, *34*(6), 409–430. https://doi.org/10.1007/s00269-007-0158-6

Dzurisin, D. (2007). *Volcano Deformation: Geodetic Monitoring Techniques*. Berlin, Germany: Springer Praxis.

Efron, B. (1982). *The jackknife, the bootstrap and other resampling plans*. Philadelphia, PA: Society for Industrial and Applied Mathematics. https://doi.org/10.1137/1.9781611970319

Fernández, J., Pepe, A., Poland, M. P., & Sigmundsson, F. (2017). Volcano geodesy: Recent developments and future challenges. *Journal of Volcanology and Geothermal Research*, *344*, 1–12. https://doi.org/10.1016/j.jvolgeores.2017.08.006

Ferrucci, F., Rasà, R., Gaudiosi, G., Azzaro, R., & Imposa, S. (1993). Mt. Etna: a model for the 1989 eruption. *Journal of Volcanology and Geothermal Research*, *56*(1–2), 35–56. https://doi.org/10.1016/0377-0273(93)90049-W

Geiger, H., Mattsson, T., Deegan, F. M., Troll, V. R., Burchardt, S., Gudmundsson, O., et al. (2016). Magma plumbing for the 2014–2015 Holuhraun eruption, Iceland. *Geochemistry, Geophysics, Geosystems*, *17*, 2953–2968. https://doi.org/10.1002/2016GC006317

Ghiorso, M. S., & Gualda, G. A. R. (2015). An H_2O-CO_2 mixed fluid solubility model compatible with rhyolite-MELTS. *Contributions to Mineralogy and Petrology*, *169*(6), 53. https://doi.org/10.1007/s00410-015-1141-8

Giampiccolo, E., Cocina, O., De Gori, P., & Chiarabba, C. (2020). Dyke intrusion and stress-induced collapse of volcano flanks: The example of the 2018 event at Mt. Etna (Sicily, Italy). *Scientific Reports*, *10*, 6373. https://doi.org/10.1038/s41598-020-63371-3

Giuffrida, M., & Viccaro, M. (2017). Three years (2011–2013) of eruptive activity at Mt. Etna: Working modes and timescales of the modern volcano plumbing system from micro-analytical studies of crystals. *Earth-Science Reviews*, *171*, 289–322. https://doi.org/10.1016/j.earscirev.2017.06.003

Giuffrida, M., Viccaro, M., & Ottolini, L. (2018). Ultrafast syn-eruptive degassing and ascent trigger high-energy basic eruptions. *Scientific Reports*, *8*, 147. https://doi.org/10.1038/s41598-017-18580-8

Gonzalez, P. J., & Palano, M. (2014). Mt. Etna 2001 eruption: New insights into the magmatic feeding system and the mechanical response of the western flank from a detailed geodetic dataset. *Journal of Volcanology and Geothermal Research*, *274*, 108–121. https://doi.org/10.1016/j.jvolgeores.2014.02.001

Gualda, G. A. R., Ghiorso, M. S., Lemons, R. V., & Carley, T. L. (2012). Rhyolite-MELTS: A modified calibration of MELTS optimized for silica-rich, fluid-bearing magmatic systems. *Journal of Petrology*, *53*(5), 875–890. https://doi.org/10.1093/petrology/egr080

Herring, T. A., King, R. W., Floyd, M. A., & McClusky, S. C. (2018). *Introduction to GAMIT/GLOBK, Release 10.70*. Cambridge: Massachusetts Institute of Technology.

Hibert, C., Mangeney, A., Polacci, M., Di Muro, A., Vergniolle, S., Ferrazzini, V., et al. (2015). Toward continuous quantification of lava extrusion rate: Results from the multidisciplinary analysis of the 2 January 2010 eruption of Piton de la Fournaise volcano, La Réunion. *Journal of Geophysical Research: Solid Earth*, *120*, 3026–3047. https://doi.org/10.1002/2014JB011769

INGV-OE Internal Report (2019). Etna Bollettino Settimanale 24/12/2018–30/12/2018, Rep. n° 01/2019, Catania, Italy, available at www.ct.ingv.it

Kahl, M., Chakraborty, S., Pompilio, M., & Costa, F. (2015). Constraints on the nature and evolution of the magma plumbing system of Mt. Etna volcano (1991–2008) from a combined thermodynamic and kinetic modelling of the compositional record of minerals. *Journal of Petrology*, *56*(10), 2025–2068. https://doi.org/10.1093/petrology/egv063

Magee, C., Stevenson, C. T. E., Ebmeier, S. K., Keir, D., Hammond, J. O. S., Gottsmann, J. H., et al. (2018). Magma plumbing systems: A geophysical perspective. *Journal of Petrology*, *59*(6), 1217–1251. https://doi.org/10.1093/petrology/egy064

Martí, J., Castro, A., Rodríguez, C., Costa, F., Carrasquilla, S., Pedreira, R., & Bolos, X. (2013). Correlation of magma evolution and geophysical monitoring during the 2011–2012 El Hierro (Canary Islands) submarine eruption. *Journal of Petrology*, *54*(7), 1349–1373. https://doi.org/10.1093/petrology/egt014

Palano, M. (2016). Episodic slow slip events and seaward flank motion at Mt. Etna volcano (Italy). *Journal of Volcanology and Geothermal Research*, *324*, 8–14. https://doi.org/10.1016/j.jvolgeores.2016.05.010

Palano, M., Rossi, M., Cannavò, F., Bruno, V., Aloisi, M., Pellegrino, D., et al. (2010). Etn@ref, a geodetic reference frame for Mt. Etna GPS networks. *Annals of Geophysics*, *53*(4), 48–79. https://doi.org/10.4401/ag-4879

Palano, M., Viccaro, M., Zuccarello, F., & Gresta, S. (2017). Magma transport and storage at Mt. Etna (Italy): A review of geodetic and petrological data for the 2002-03, 2004 and 2006 eruptions. *Journal of Volcanology and Geothermal Research*, *347*, 149–164. https://doi.org/10.1016/j.jvolgeores.2017.09.009

Pezzo, G., Palano, M., Tolomei, C., De Gori, P., Calcaterra, S., Gambino, P., & Chiarabba, C. (2020). Flank sliding: A valve and a sentinel for paroxysmal eruptions and magma ascent at Mount Etna, Italy. *Geology*, *48*. https://doi.org/10.1130/G47656.1

Saastamoinen, J. (1972). Contribution to the theory of atmospheric refraction. *Bulletin of Geodesy*, *105*(1), 279–298. https://doi.org/10.1007/BF02521844

Shea, T., Costa, F., Krimer, D., & Hammer, J. E. (2015). Accuracy of timescales retrieved from diffusion modeling in olivine: A 3D perspective. *American Mineralogist*, *100*(10), 2026–2042. https://doi.org/10.2138/am-2015-5163

Tiampo, K. F., Rundle, J. B., Fernandez, J., & Langbein, J. O. (2000). Spherical and ellipsoidal volcanic sources at Long Valley caldera, California, using a genetic algorithm inversion technique. *Journal of Volcanology and Geothermal Research*, *102*(3–4), 189–206. https://doi.org/10.1016/S0377-0273(00)00185-2

Viccaro, M., Barca, D., Bohrson, W. A., D'Oriano, C., Giuffrida, M., Nicotra, E., & Pitcher, B. W. (2016). Crystal residence times from trace element zoning in plagioclase reveal changes in magma transfer dynamics at Mt. Etna during the last 400 years. *Lithos*, *248–251*, 309–323. https://doi.org/10.1016/j.lithos.2016.02.004

Viccaro, M., Calcagno, R., Garozzo, I., Giuffrida, M., & Nicotra, E. (2015). Continuous magma recharge at Mt. Etna during the 2011–2013 period controls the style of volcanic activity and compositions of erupted lavas. *Mineralogy and Petrology*, *109*(1), 67–83. https://doi.org/10.1007/s00710-014-0352-4

Viccaro, M., Garozzo, I., Cannata, A., Di Grazia, G., & Gresta, S. (2014). Gas burst vs. gas-rich magma recharge: A multidisciplinary study to reveal factors controlling triggering of the recent paroxysmal eruptions at Mt. Etna. *Journal of Volcanology and Geothermal Research*, *278–279*, 1–13. https://doi.org/10.1016/j.jvolgeores.2014.04.001

Viccaro, M., Giuffrida, M., Zuccarello, F., Scandura, M., Palano, M., & Gresta, S. (2019). Violent paroxysmal activity drives self-feeding magma replenishment at Mt. Etna. *Scientific Reports*, *9*(1), 6717. https://doi.org/10.1038/s41598-019-43211-9

Viccaro, M., Zuccarello, F., Cannata, A., Palano, M., & Gresta, S. (2016). How a complex basaltic volcanic system works: Constraints from integrating seismic, geodetic, and petrological data at Mount Etna volcano during the July–August 2014 eruption. *Journal of Geophysical Research: Solid Earth*, *121*, 5659–5678. https://doi.org/10.1002/2016JB013164

Williams, C. A., & Wadge, G. (2000). An accurate and efficient method for including the effects of topography in three-dimensional elastic models of ground deformation with applications to radar interferometry. *Journal of Geophysical Research*, *105*(B4), 8103–8120. https://doi.org/10.1029/1999JB900307

Yang, X. M., Davis, P. M., & Dieterich, J. H. (1988). Deformation from inflation of a dipping finite prolate spheroid in an elastic half-space as a model for volcanic stressing. *Journal of Geophysical Research*, *93*(B5), 4249–4257. https://doi.org/10.1029/JB093iB05p04249